

Transverse voltage in anisotropic hydrodynamic conductors

Kaize Wang,^{1,*} Chunyu Guo,¹ Philip J. W. Moll,^{1,†} and Tobias Holder^{2,‡}

¹Max Planck Institute for the Structure and Dynamics of Matter, Hamburg 22761, Germany

²School of Physics and Astronomy, Tel Aviv University, Tel Aviv 69978, Israel

(Dated: September 25, 2024)

Weak momentum dissipation in ultra-clean metals gives rise to novel non-Ohmic current flow, including ballistic and hydrodynamic regimes. Recently, hydrodynamic flow has attracted intense interest because it presents a valuable window into the electronic correlations and the longest lived collective modes of quantum materials. However, diagnosing viscous flow is difficult as the macroscopic observables of ballistic and hydrodynamic transport such as the average current distribution can be deceptively similar, even if their respective microscopies deviate notably. Based on kinetic Boltzmann theory, here we propose to address this issue via the transverse channel voltage at zero magnetic field, which can efficiently detect hydrodynamic flow in a number of materials. To this end, we show that the transverse voltage is sensitive to the interplay between anisotropic fermiology and boundary scattering, resulting in a non-trivial behavior in narrow channels along crystalline low-symmetry directions. We discuss several materials where the channel-size dependent stress of the quantum fluid leads to a characteristic sign change of the transverse voltage as a new hallmark of the cross-over from the ballistic to the hydrodynamic regime.

Introduction.— Hydrodynamic electron flow is a special transport regime which onsets when a rapid electron-electron scattering rate exceeds all other relaxation mechanisms. In recent years, its fundamental importance became apparent in understanding the longest lived collective modes of correlated electrons [1–4]. For example, viscous (hydrodynamic) correlations can shed light on electronic collective behavior, on the interacting phase diagram, and reveal unusual characteristics in the electron dynamics [5–7]. Hydrodynamic electron flow has also been discussed in connection to THz electromagnetic radiation in transistors [8–10], ambipolar transports in semiconductors/semimetals [11–13] and fluid spintronics [14–17]. The current conceptual frontiers of interacting Fermi liquids are found in understanding correlations on the nanoscale, either due to extreme scattering rates in strongly correlated electron systems such as high- T_c superconductors, or due to nanoconfinement in heterostructures such as the nanoscopic channel sizes of current transistors. Advancing these goals necessitates experimental approaches sensing momentum diffusion in confined conductors. The last few years saw tremendous experimental progress in the imaging [18–23] and characterization [4, 24–26] of the crossover regime between hydrodynamic and ballistic flow. At the same time, these efforts have also revealed that the actual flow profile of a quantum fluid in thin channels is rather ambiguous with respect to the dominant relaxation mechanism [27]. While it is possible to alleviate this issue by choosing other geometries [21, 28–30] or measure at finite magnetic field [31, 32], identifying more easily accessible characteristics which are sensitive to the ballistic-hydrodynamic crossover is highly sought after. The key point of this paper is to establish the transverse channel voltage in anisotropic conductors as such an accessible characteristic.

acterized by three characteristic length scales [33]: The system size W , the momentum-relaxing (MR) mean-free path ℓ_{mr} , and the momentum-conserving (MC) mean-free path ℓ_{mc} . In very clean systems it holds that $W \ll \ell_{\text{mr}}$ and Ohm's law no longer describes the local relationship between electric field and current. The system therefore becomes ballistic if $W \ll \ell_{\text{mr}} \ll \ell_{\text{mc}}$ or hydrodynamic if $\ell_{\text{mc}} \ll W \ll \ell_{\text{mr}}$ (Fig. 1a).

In previous studies, the crossover regime (Gurzhi regime) when all three length scales are comparable ($W \approx \ell_{\text{mr}} \approx \ell_{\text{mc}}$) has been studied theoretically by a Boltzmann kinetic approach with a Callaway two-rate ansatz for isotropic Fermi surfaces [32–35]. The implicit assumption for this starting point is that the simplified isotropic description ought to capture the qualitative features of the ballistic-hydrodynamic crossover. However, this is far from obvious: From the point of view of theory, the limited attention to anisotropic effects means that essential parts of the kinetic approach have never been developed to take into account viscous correlations in an anisotropic system. Experimentally, it is important to investigate the sensitivity of observables such as flow profiles against inevitable misalignments between the channel and the crystal axes. Since several candidate materials with hydrodynamic electronic transport are in fact metals with anisotropic Fermi surfaces [19, 24, 36], it is critical to investigate the effect of symmetry breaking through the channel walls on the often subtle signatures of hydrodynamic flow. One might even ask if the Fermi surface shape can provide valuable insight for the ballistic-hydrodynamic crossover of a quantum fluid. Theoretical efforts to explore anisotropic effects in hydrodynamic conductors include broadband microwave spectroscopy [37, 38], a non-monotonic temperature and width dependence of the channel conductance [39], and viscous flow profiles on a Corbino disk [40].

Electron transport in mesoscopic conductors is char-

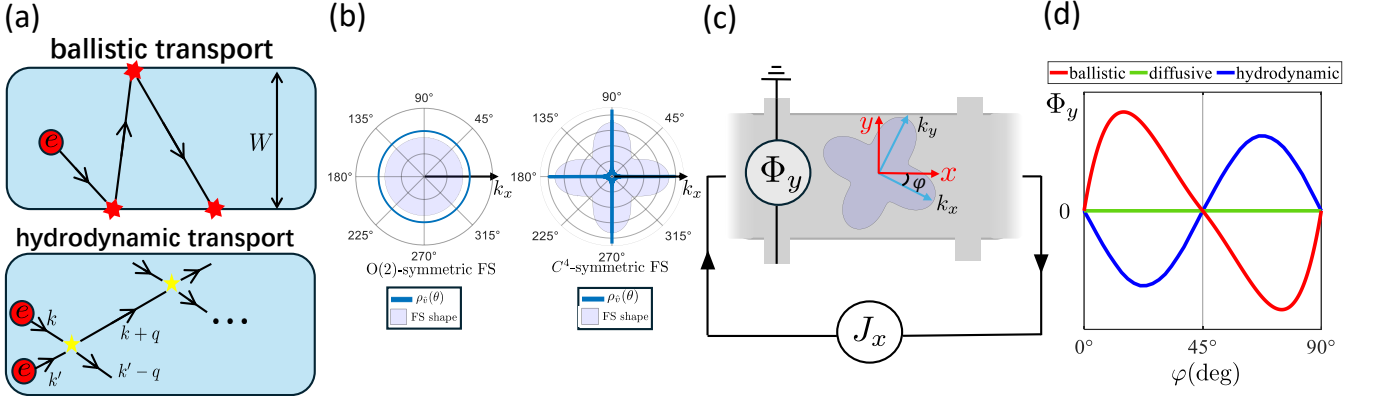


Figure 1. (a) Ballistic and hydrodynamic transport regimes. The red star represents scattering events with the boundary, while a yellow one represents the MC two-body scattering between electrons. (b) Representative Fermi surfaces with continuous rotational symmetry and with anisotropy. ρ_v denotes the distribution of Fermi velocity directions, shown in a polar histogram. (c) A four point geometry for measurements of transverse voltages with misalignment angle φ between the crystal principle axis and the channel direction. (d) Schematics of the transverse voltage as a function of misalignment angle in different regimes for a Fermi surface with C_4 symmetry.

Here, we address this question by examining the transverse voltage in the absence of magnetic field. Our main focus is anisotropic systems (Fig. 1b) lacking mirror symmetry due to a directional mismatch between the high symmetry axis of the Fermi surface and the geometric axis of the channel (Fig. 1c). To describe these systems, we generalise the Callaway ansatz to any two-dimensional anisotropic system, finding that a transverse voltage emerges at zero magnetic field which is strongly sensitive to the microscopic scattering mechanism. In particular, we show that the sign of the transverse voltage depends both on the Fermi surface shape and also the MC scattering rate. Under certain conditions, a sign reversal can indicate that the system crosses over from ballistic to hydrodynamic flow (Fig. 1d), which can serve as a sensitive observable for the crossover. We explain these subtle changes as the result of a competition of the transverse stress induced by the boundaries against the stress resulting from the bulk MR scattering. Using the sign to identify the onset of hydrodynamic regimes offers several advantages. Firstly, it only requires a non-spatially resolved transport measurement of a single device. Secondly, the sign change of the transverse voltage is uncommon outside the hydrodynamic context, as in other regimes, it typically only relates to the carrier type of the material. Although the sign change strongly suggests a crossover, it does not mark a precise boundary between the ballistic and hydrodynamic regimes, as this is not a phase transition. In short, we suggest the signature of the transverse voltage as a relatively straightforward experimental observable for detecting non-local hydrodynamic transport. Additionally, our work establishes a general framework to treat anisotropic ballistic and hydrodynamic transport in systems with C_4 rotational symmetry or higher.

Collisional invariants for anisotropic Fermi surfaces.—

We aim to describe the ballistic-hydrodynamic crossover using semiclassical kinetics. The starting point is the Boltzmann transport equation (BTE) for the distribution function f , given by $(\partial_t + \mathbf{v}_\mathbf{k} \cdot \nabla_\mathbf{r} + \mathbf{F} \cdot \nabla_\mathbf{k})f(\mathbf{r}, \mathbf{p}, t) = C[f(\mathbf{r}, \mathbf{p}, t)]$, where C is the collision integral and \mathbf{F} is the perturbation. It is common to parametrize the deviation from the equilibrium state by writing $f(\mathbf{r}, \mathbf{p}, t) - f^0(\varepsilon_\mathbf{p}) = -E_F \partial_\varepsilon f^0(\varepsilon) h(\mathbf{r}, \mathbf{p}, t)$, where E_F is the Fermi energy and h is dimensionless non-equilibrium distribution function. In the following, we consider the low temperature limit where $\partial_\varepsilon f^0(\varepsilon) \approx -\delta(\varepsilon - E_F)$. This is a good assumption for materials with a large carrier density since the actual temperature is significantly lower than the Fermi temperature. In experiment, variations in temperature usually have a greater impact on the scattering rate than on the thermal broadening of the distribution function. For the sake of simplicity, we consider a Fermi surface for which a bijection between angular variable θ and Fermi wave vector \mathbf{p}_F exists. This allows to integrate out the radial momentum dependence of \mathbf{p} , leaving only an angular momentum variable θ . In more general scenarios, the Fermi surface arclength should be employed instead.

We begin by defining a bra-ket notation for the BTE [37, 39, 41]. Let $g(\mathbf{r}, \theta, t)$ be a state function on the Fermi surface. Then the corresponding ket and inner product in two-dimension are defined by

$$|g(\mathbf{r}, t)\rangle = \int d\theta \sqrt{\frac{p_F^2(\theta) E_F}{(2\pi\hbar)^2 |\mathbf{v}_F(\theta) \cdot \mathbf{p}_F(\theta)|}} g(\mathbf{r}, \theta, t) |\theta\rangle \chi(1)$$

where $\langle \theta | \theta' \rangle = \delta(\theta - \theta')$. With this definition, $\langle g(\mathbf{r}, t) | = \langle h(\mathbf{r}, t) | g(\mathbf{r}, t) \rangle$.

For convenience, we abbreviate the metric in phase space as $A(\theta) = p_F^2(\theta) E_F / (2\pi\hbar)^2 |\mathbf{v}_F(\theta) \cdot \mathbf{p}_F(\theta)|$ and define the following modes with unit length: A particle

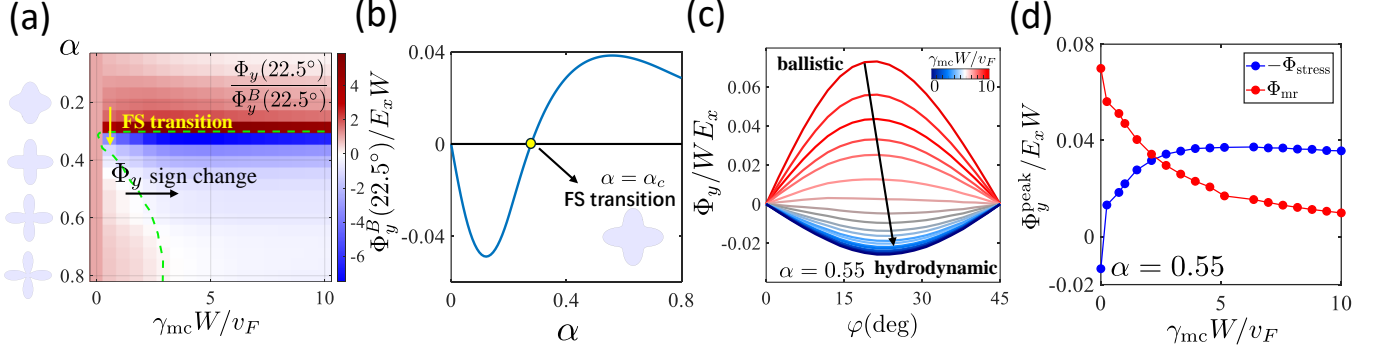


Figure 2. (a) Transverse voltage at 22.5° normalized by the ballistic value, shown as a function of both Fermi surface anisotropy α and dimensionless MC rate. Green dotted line: interpolated boundary line when transverse voltage is vanishing. Yellow arrow: Fermi surface transition happens at $\alpha \approx 0.3$, corresponding to a sign-change of ballistic transverse voltage, black arrow: a line-cut for a fixed Fermi surface, where transverse voltage changes sign with increase MC rate. (b) Ballistic transverse voltage as a function of α . Yellow dot: non-trivial zero of the ballistic transverse voltage signifying the Fermi surface transition. (c) Transverse voltage as a function of misalignment angle φ , parameters are taken as indicated by the black line cut in (a). From ballistic to hydrodynamic region, the transverse voltage flips its sign. (d) Decomposition of the transverse voltage. As MC rate increases, MR contribution is decreasing to zero and the stress component is dominant.

mode called $|c\rangle \propto \int d\theta \sqrt{A(\theta)} |\theta\rangle$, corresponding to the particle number, and a momentum mode called $|p_\mu\rangle \propto \int d\theta \sqrt{A(\theta)} p_\mu(\theta) |\theta\rangle$, which will be relevant for contractions which preserve momentum [24, 33, 37, 39, 41, 42].

To proceed, we need to make some assumptions about the collisional integral C . Here, we take the Callaway two-rate ansatz [34] to construct phenomenological collisional terms. The idea is to restrict C to an universal subset of eigenmodes which are longest lived. For electron flow in a channel, these long-lived modes derive from particle number which is conserved exactly and momentum, which relaxes with a small scattering rate γ_{mr} . Assuming that all other excitations relax at least as fast as these quasi-conserved quantities with rate $\gamma = \gamma_{\text{mc}} + \gamma_{\text{mr}}$ [37, 39], one obtains two collisional integrals,

$$\begin{aligned} C_{\text{mr}} &= -\gamma_{\text{mr}}(\mathbb{1} - |c\rangle\langle c|), \\ C_{\text{mc}} &= -\gamma_{\text{mc}} \left(\mathbb{1} - |c\rangle\langle c| - \sum_{\mu} |p_\mu\rangle\langle p_\mu| \right). \end{aligned} \quad (2)$$

Importantly, as long as $W \ll v_F/\gamma_{\text{mr}}$, this construction guarantees both particle number and (approximate) momentum conservation since $\langle c|C_{\text{mr/mc}}|h\rangle = 0$ and $\langle p_\mu|C_{\text{mc}}|h\rangle = 0$.

Let us consider the transverse transport in a long narrow channel geometry (Fig. 1) at zero magnetic field and zero temperature. This geometry is assumed to be translationally invariant in the longitudinal direction (denoted x), thus the distribution function only has a spatial dependence in y direction. As a function of the remaining two parameters (y, θ) ,

the Boltzmann equation becomes,

$$D[h] = (C_{\text{mr}} + C_{\text{mc}})|h\rangle, \quad (3)$$

where the drift terms are

$$D[h] = \partial_y |v_y h\rangle - E_x |v_x\rangle - E_y |v_y\rangle. \quad (4)$$

Here, E_x, E_y are electric fields normalized by the Fermi energy, having the same unit as a wave vector. We assume a fixed longitudinal electric field E_x and view $E_y(y)$ as a response to the input field E_x .

Rearranging terms, one obtains

$$\begin{aligned} C_0|h\rangle &= \sum_{\mu} E_{\mu} |v_{\mu}\rangle \\ &+ \left[\gamma |c\rangle\langle c| + \gamma_{\text{mc}} \sum_{\nu} |p_{\nu}\rangle\langle p_{\nu}| \right] |h\rangle, \end{aligned} \quad (5)$$

where $C_0|h\rangle = \partial_y |v_y h\rangle + \gamma|h\rangle$. A proper diffusive boundary condition is imposed as $h^\pm(\mp W/2, \theta) = 0$ and $J_y(y) \equiv \langle v_y |h\rangle = 0$. Here, $h^\pm(y, \theta)$ are $h(y, \theta)$ restricted to the domain $\Theta^\pm = \{\theta | \text{sign}[v_y(\theta)] = \pm 1\}$ respectively.

In this form, we can solve the BTE self-consistently and obtain the transverse electric field as $E_y(y) = \langle p_y |v_y\rangle^{-1} (\langle p_y |C_0|h\rangle - \gamma_{\text{mc}} \sum_{\mu} \langle h |p_\mu\rangle \langle p_\mu |v_y\rangle)$. The transverse voltage is the integral $\Phi_y = \int dy E_y(y)$. We can clearly identify two different components in Φ_y , which read explicitly $\Phi_y = \Phi_y^{\text{stress}} + \Phi_y^{\text{mr}}$, where

$$\begin{aligned} \Phi_y^{\text{stress}} &= \langle p_y |v_y\rangle^{-1} \langle p_y |v_y h\rangle \Big|_{-W/2}^{W/2} \\ \Phi_y^{\text{mr}} &= \langle p_y |v_y\rangle^{-1} \gamma_{\text{mr}} \int_{-W/2}^{W/2} dy \langle p_y |h\rangle \end{aligned} \quad (6)$$

Here, Φ_y^{stress} is related to the yy component of the stress tensor $\Pi_{\mu\nu} \equiv \langle p_\mu |v_\nu h\rangle$ of the quantum fluid, whereas Φ_y^{mr} is proportional to the MR rate γ_{mr} .

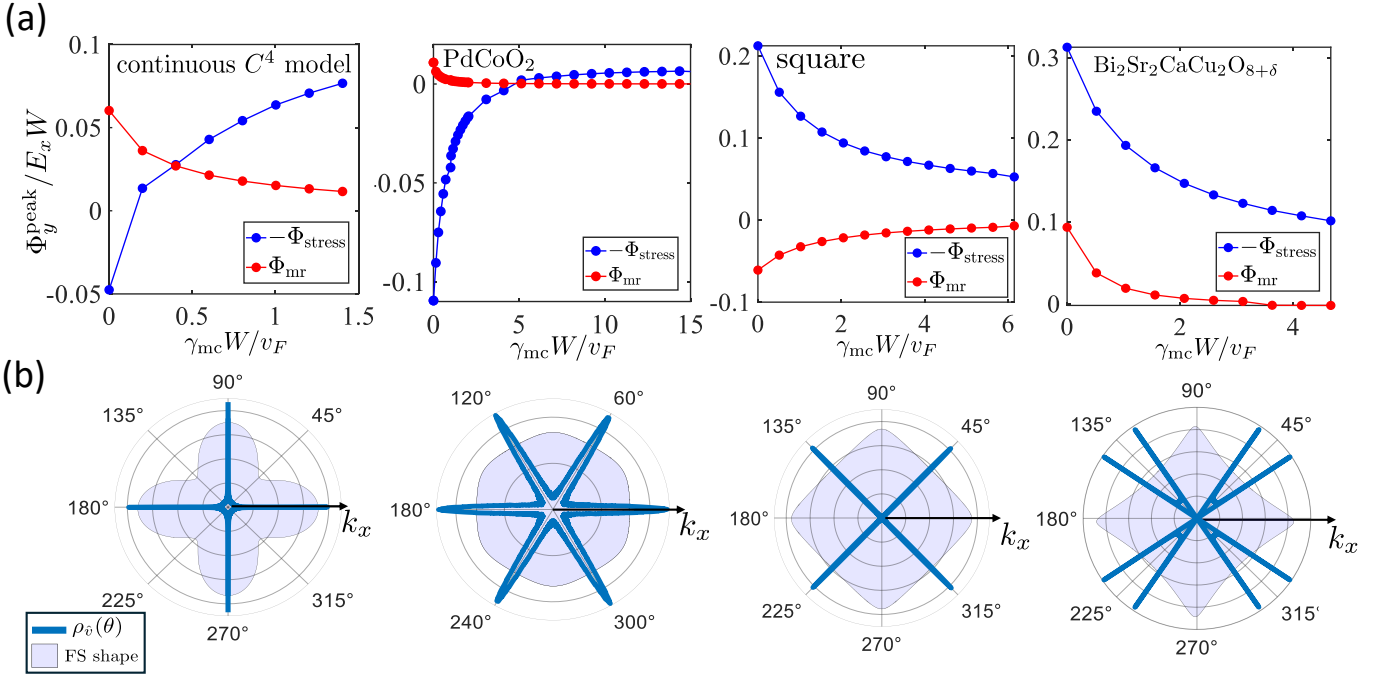


Figure 3. (a) Decomposition of the transverse voltage of different models. Left to right: C_4 model with a energy dispersion $\varepsilon(k)$ with $\gamma_{\text{mr}}W/v_F = 0.1$ [42], TB model for PdCoO₂ [43] with $\gamma_{\text{mr}}W/v_F = 0.08$, TB square model with $\gamma_{\text{mr}}W/v_F = 0.49$ [42], TB model for over-doped cuprate Bi2212 [44] with $\gamma_{\text{mr}}W/v_F = 0.49$. (b) Fermi velocity direction distribution plotted as a polar histogram plot.

Ballistic-hydrodynamic crossover.— In order to demonstrate the anisotropy effect of Fermi surface in a tractable manner, we use the following parameterization for the Fermi wave vector k_F for a C_n Fermi surface $k_F(\theta; \alpha, \varphi) = k_F^0 \{1 + \alpha \cos[n(\theta - \varphi)]\}$, where θ is the angle between \mathbf{k}_F and the crystal k_x -axis, φ is the angle between the crystal and channel axes as shown in Fig.2a. α is the controlling parameter for the Fermi surface shape. With varying α , the Fermi surface goes from circular to cross-shaped, and finally flower-shaped, as shown in Fig.2a for $n = 4$.

We mainly focus on non-Ohmic region, so we fix the MR rate γ_{mr} within the limit $\gamma_{\text{mr}}W/v_F \lesssim 1$ and change the MC rate γ_{mc} to investigate the ballistic-hydrodynamic crossover. The transverse voltage at the misalignment angle $\varphi = 22.5^\circ$ which marks the maximal transverse voltage in the ballistic case as a function of both Fermi surface shape and MC scattering rate is studied in Fig.2(a). In order to show the sign change of the transverse voltage, it is best to look at the normalized quantity Φ_y/Φ_B where Φ_B is the ballistic voltage ($\gamma_{\text{mc}} = 0$). We observe that for a fixed small $\alpha < \alpha_c$, the transverse voltage remains of the same sign irrespective of the value of γ_{mc} . At the critical value $\alpha_c \approx 0.3$, the increasingly anisotropic Fermi surface leads to a sign change of the ballistic voltage (yellow arrow). We should emphasize that the sign reverses when changing the Fermi surface is not due to the hydrodynamic nature, it is a direct consequence of the Fermi velocity distribution of different Fermi surfaces. In

the supplemental material [42], we show that this latter sign change is determined by the quantity $\langle v_x \text{sign}(v_y) \rangle$. The physical picture is that for a given driven electric field E_x , the response to it is proportional to v_x , and $\text{sign}(v_y)$ indicates the electrons moving to the top or bottom in the transverse direction of the channel.

More interestingly, for a fixed large $\alpha > \alpha_c$, with increasing MC scattering rate γ_{mc} , the voltage exhibits an additional sign change between the ballistic region and the hydrodynamic region (cf. green dotted line in Fig. 2a). This latter sign change persists for basically all misalignment angles, as is shown in Fig. 2c. We can conclude that during the ballistic-hydrodynamic crossover, some anisotropic Fermi surfaces will cause the modulus of the transverse voltage to first decrease, cross zero smoothly and then increase with opposite sign. We further observe that $\Phi_y(\varphi)$ can have a quite asymmetric shape, which changes noticeably as a function of γ_{mc} . As mentioned above Eq. (6), we want to understand the underlying mechanism for the transverse voltage by decomposing the voltage as an internal stress contribution and MR contribution. The two contributions to the stress are shown in Fig. 2d for the anisotropy parameter $\alpha = 0.55$. Φ_y here is taken as the peak voltage in the whole range of φ rotation at a fixed γ_{mr} and varying with γ_{mc} . In essence, in the hydrodynamic regime such that $\gamma_{\text{mc}}W/v_F \gg 1$, the MR component is vanishing so that the the internal stress of the quantum fluid becomes the dominant contribution to

the transverse voltage. Conversely, the dissipative stress dominates at small γ_{mc} , therefore there exists a critical γ_{mc}^c where the two contributions cancel and the sign of transverse voltage Φ_y reverses.

Material examples.— Here we present some instructive examples of anisotropic Fermi surfaces which additionally contain anisotropic Fermi velocities. We find that both a continuum model and tight-binding(TB) examples can exhibit a behavior very similar to the one discussed for the simplified scenario, thus confirming the robustness of our diagnosis. Namely, we focus on the ultra clean material PdCoO₂ [24], and the overdoped strongly correlated cuprate Bi₂Sr₂CaCu₂O_{8+ δ} (Bi2212) [36], as in both non-Ohmic transport has been observed. For comparison, we also include a square lattice with nearest-neighbor hopping. The model details can be found in the supplemental material [42], the results of these calculations are shown in Fig. 3. Not surprisingly, in all cases the MR component is diminishing when approaching the hydrodynamic limit. Thus in the hydrodynamic region, the only contribution to transverse voltage is the yy component of the stress tensor $\Pi_{\mu\nu}$. For the anisotropic C_4 model [42], our calculation reveals a sign change of the transverse voltage with increasing MC scattering rate, serving as a direct indicator of hydrodynamic transport. The location of this crossover, however, depends on the Fermi surface shape, the channel width, and the el-el scattering rate. For the Fermi surfaces of the square and Bi2212, for example, such a sign change would occur at extreme scattering rates inaccessible to our numerical implementation. Thus in a real material, these parameters may render the sign change inaccessible for realistic channel sizes.

This diagnostic methodology can be extended to treat those situations, thus greatly expanding its range of applicability. The transverse voltage results from a competition between Φ_y^{stress} and Φ_y^{mr} , which in general scale differently with the channel misalignment angle φ (see asymmetry evolution in Fig. 2c). Hence the transverse voltage difference between two channels symmetrically misaligned by an angle $\pm\delta\varphi$ to mutually adjacent mirror planes is a sensitive probe of emergent hydrodynamics (Fig 4). Its asymmetry is actually most pronounced in the weakly hydrodynamic sector of small $\gamma_{mc}W/v_F$ and a channel width dependence allows a straightforward estimation of γ_{mc} through a transport experiment. The required simple geometry of two canted bars is sketched in Fig. 4a. Varying the channel width by a factor of 10 is straightforward lithographically, which will provide enough range to extract γ_{mc} even when the sign change itself cannot be accessed.

Conclusion.— By employing a Callaway two-rate ansatz, we have identified a non-vanishing transverse voltage for a wide range of low-symmetry transport configurations. We find that in a C_4 -symmetric system, a sufficiently anisotropic Fermi surface can lead to a sign change in the transverse voltage as the electron fluid

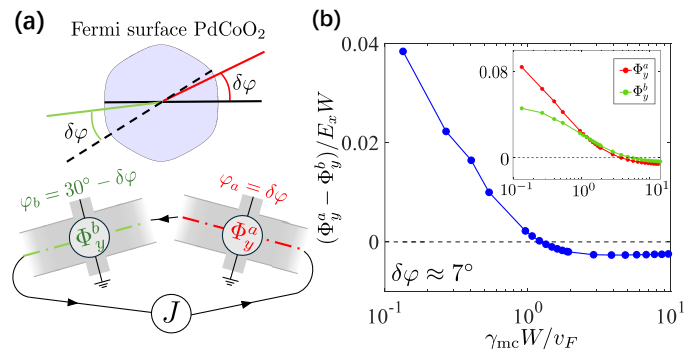


Figure 4. (a) Sketch for measurement of the difference of transverse voltage $\Phi_y^a - \Phi_y^b$ at misalignment angle $\varphi_a = \delta\varphi$ and $\varphi_b = 30^\circ - \delta\varphi$ for PdCoO₂. (b) Difference of transverse voltage as function of MC scattering rate. Inset: Φ_y^a and Φ_y^b as a function of MC scattering rate.

crosses over from ballistic to hydrodynamic transport. We therefore propose that measuring the transverse voltage at zero magnetic field can be a viable way to distinguish different types of non-Ohmic transport. The prescribed phenomenology offers an alternative probe for the experimental investigation of unconventional charge transport beyond the analysis of the current flow pattern. We reiterate that the measurement of transverse voltage seems particularly attractive because it does not require an external magnetic field or a local imaging of the current profile. We believe that the sign change is observable with current devices as a function of either gate voltage or temperature using the geometry depicted in Fig. 4. For example, in Ref. [24], the estimated range of γ_{mr}/γ_{mc} is $0.05 \sim 0.2$, based on fits of the conductivity to an isotropic model.

As a limitation of our results, let us mention that the simplifications to the collision integral used here cannot capture the intermediate tomographic transport regime [41, 45–47]. Further refinements in the treatment of the full collision integral seem needed to treat these and similar effects in anisotropic materials. On the other hand, the methodology developed here can be extended straightforwardly to investigate hydrodynamic crossovers in three-dimensional systems.

T.H. acknowledges financial support by the European Research Council (ERC) under grant QuantumCUSP (Grant Agreement No. 101077020).

* kaize.wang@mpsd.mpg.de
 † philip.moll@mpsd.mpg.de
 ‡ tobiasholder@tauex.tau.ac.il

- [1] A. Lucas and K. Chung Fong, Hydrodynamics of electrons in graphene, *J. Phys. Cond. Matter* **30**, 053001 (2018).
- [2] B. N. Narozhny, Hydrodynamic approach to two-dimensional electron systems, *Nuovo Cimento Rivista*

- Serie **45**, 661 (2022).
- [3] G. Varnavides, A. Yacoby, C. Felser, and P. Narang, Charge transport and hydrodynamics in materials, *Nature Reviews Materials* **8**, 726 (2023).
- [4] L. Fritz and T. Scaffidi, Hydrodynamic electronic transport, *Annu. Rev. Condens. Matter Phys.* **15**, 17 (2024).
- [5] P. K. Kovtun, D. T. Son, and A. O. Starinets, Viscosity in Strongly Interacting Quantum Field Theories from Black Hole Physics, *Phys. Rev. Lett.* **94**, 111601 (2005).
- [6] B. N. Narozhny and A. Levchenko, Coulomb drag, *Rev. Mod. Phys.* **88**, 025003 (2016).
- [7] S. A. Hartnoll, A. Lucas, and S. Sachdev, *Holographic Quantum Matter* (MIT Press, 2018).
- [8] J. H. Farrell, N. Grisouard, and T. Scaffidi, Terahertz radiation from the dyakonov-shur instability of hydrodynamic electrons in corbino geometry, *Phys. Rev. B* **106**, 195432 (2022).
- [9] J. Crabb, X. Cantos-Roman, J. M. Jornet, and G. R. Aizin, Hydrodynamic theory of the dyakonov-shur instability in graphene transistors, *Phys. Rev. B* **104**, 155440 (2021).
- [10] M. Dyakonov and M. Shur, Shallow water analogy for a ballistic field effect transistor: New mechanism of plasma wave generation by dc current, *Phys. Rev. Lett.* **71**, 2465 (1993).
- [11] C. Tan, D. Y. H. Ho, L. Wang, J. I. A. Li, I. Yudhistira, D. A. Rhodes, T. Taniguchi, K. Watanabe, K. Shepard, P. L. McEuen, C. R. Dean, S. Adam, and J. Hone, Dissipation-enabled hydrodynamic conductivity in a tunable bandgap semiconductor, *Science Advances* **8**, eabi8481 (2022).
- [12] Y. Nam, D.-K. Ki, D. Soler-Delgado, and A. F. Morpurgo, Electron-hole collision limited transport in charge-neutral bilayer graphene, *Nature Physics* **13**, 1207 (2017).
- [13] C. A. Kukkonen and P. F. Maldague, Electron-hole scattering and the electrical resistivity of the semimetal TiS_2 , *Phys. Rev. Lett.* **37**, 782 (1976).
- [14] M. Matsuo, Y. Ohnuma, and S. Maekawa, Theory of spin hydrodynamic generation, *Phys. Rev. B* **96**, 020401 (2017).
- [15] R. Takahashi, M. Matsuo, M. Ono, K. Harii, H. Chudo, S. Okayasu, J. Ieda, S. Takahashi, S. Maekawa, and E. Saitoh, Spin hydrodynamic generation, *Nature Physics* **12**, 52 (2016).
- [16] R. Takahashi, H. Chudo, M. Matsuo, K. Harii, Y. Ohnuma, S. Maekawa, and E. Saitoh, Giant spin hydrodynamic generation in laminar flow, *Nature Communications* **11**, 3009 (2020).
- [17] G. Tatara, Hydrodynamic theory of vorticity-induced spin transport, *Phys. Rev. B* **104**, 184414 (2021).
- [18] M. J. H. Ku, T. X. Zhou, Q. Li, Y. J. Shin, J. K. Shi, C. Burch, L. E. Anderson, A. T. Pierce, Y. Xie, A. Hamo, U. Vool, H. Zhang, F. Casola, T. Taniguchi, K. Watanabe, M. M. Fogler, P. Kim, A. Yacoby, and R. L. Walsworth, Imaging viscous flow of the Dirac fluid in graphene, *Nature* **583**, 537 (2020).
- [19] U. Vool, A. Hamo, G. Varnavides, Y. Wang, T. X. Zhou, N. Kumar, Y. Dovzhenko, Z. Qiu, C. A. C. Garcia, A. T. Pierce, J. Gooth, P. Anikeeva, C. Felser, P. Narang, and A. Yacoby, Imaging phonon-mediated hydrodynamic flow in WTe_2 , *Nat. Phys.* **17**, 1216 (2021).
- [20] L. Ella, A. Rozen, J. Birkbeck, M. Ben-Shalom, D. Perello, J. Zultak, T. Taniguchi, K. Watanabe, A. K. Geim, S. Ilani, and J. A. Sulpizio, Simultaneous imaging of voltage and current density of flowing electrons in two dimensions, *Nat. Nanotechnol.* **14**, 480 (2019).
- [21] C. Kumar, J. Birkbeck, J. A. Sulpizio, D. Perello, T. Taniguchi, K. Watanabe, O. Reuven, T. Scaffidi, A. Stern, A. K. Geim, and S. Ilani, Imaging hydrodynamic electrons flowing without Landauer-Sharvin resistance, *Nature* **609**, 276 (2022).
- [22] A. Aharon-Steinberg, A. Marguerite, D. J. Perello, K. Bagani, T. Holder, Y. Myasoedov, L. S. Levitov, A. K. Geim, and E. Zeldov, Long-range nontopological edge currents in charge-neutral graphene, *Nature* **593**, 528 (2021).
- [23] A. Jenkins, S. Baumann, H. Zhou, S. A. Meynell, Y. Daipeng, K. Watanabe, T. Taniguchi, A. Lucas, A. F. Young, and A. C. Bleszynski Jayich, Imaging the breakdown of ohmic transport in graphene, *Phys. Rev. Lett.* **129**, 087701 (2022).
- [24] P. J. W. Moll, P. Kushwaha, N. Nandi, B. Schmidt, and A. P. Mackenzie, Evidence for hydrodynamic electron flow in PdCoO_2 , *Science* **351**, 1061 (2016).
- [25] N. Nandi, T. Scaffidi, P. Kushwaha, S. Khim, M. E. Barber, V. Sunko, F. Mazzola, P. D. C. King, H. Rosner, P. J. W. Moll, M. König, J. E. Moore, S. Hartnoll, and A. P. Mackenzie, Unconventional magneto-transport in ultrapure PdCoO_2 and PtCoO_2 , *npj Quantum Materials* **3**, 66 (2018).
- [26] J. Gooth, F. Menges, N. Kumar, V. Süß, C. Shekhar, Y. Sun, U. Drechsler, R. Zierold, C. Felser, and B. Gotsmann, Thermal and electrical signatures of a hydrodynamic electron fluid in tungsten diphosphide, *Nat. Commun.* **9**, 4093 (2018).
- [27] J. A. Sulpizio, L. Ella, A. Rozen, J. Birkbeck, D. J. Perello, D. Dutta, M. Ben-Shalom, T. Taniguchi, K. Watanabe, T. Holder, R. Queiroz, A. Principi, A. Stern, T. Scaffidi, A. K. Geim, and S. Ilani, Visualizing Poiseuille flow of hydrodynamic electrons, *Nature* **576**, 75 (2019).
- [28] A. Aharon-Steinberg, T. Völkl, A. Kaplan, A. K. Pariari, I. Roy, T. Holder, Y. Wolf, A. Y. Meltzer, Y. Myasoedov, M. E. Huber, B. Yan, G. Falkovich, L. S. Levitov, M. Hücker, and E. Zeldov, Direct observation of vortices in an electron fluid, *Nature* **607**, 74 (2022).
- [29] A. Stern, T. Scaffidi, O. Reuven, C. Kumar, J. Birkbeck, and S. Ilani, How Electron Hydrodynamics Can Eliminate the Landauer-Sharvin Resistance, *Phys. Rev. Lett.* **129**, 157701 (2022).
- [30] D. A. Bandurin, A. V. Shytov, L. S. Levitov, R. K. Kumar, A. I. Berdyugin, M. Ben Shalom, I. V. Grigorieva, A. K. Geim, and G. Falkovich, Fluidity onset in graphene, *Nat. Commun.* **9**, 4533 (2018).
- [31] Y. Huang and M. Wang, Nonnegative magnetoresistance in hydrodynamic regime of electron fluid transport in two-dimensional materials, *Phys. Rev. B* **104**, 155408 (2021).
- [32] T. Scaffidi, N. Nandi, B. Schmidt, A. P. Mackenzie, and J. E. Moore, Hydrodynamic Electron Flow and Hall Viscosity, *Phys. Rev. Lett.* **118**, 226601 (2017).
- [33] M. J. M. de Jong and L. W. Molenkamp, Hydrodynamic electron flow in high-mobility wires, *Phys. Rev. B* **51**, 13389 (1995).
- [34] J. Callaway, Model for lattice thermal conductivity at low temperatures, *Phys. Rev.* **113**, 1046 (1959).
- [35] T. Holder, R. Queiroz, T. Scaffidi, N. Silberstein, A. Rozen, J. A. Sulpizio, L. Ella, S. Ilani, and A. Stern, Ballistic and hydrodynamic magnetotransport in narrow

- channels, *Phys. Rev. B* **100**, 245305 (2019).
- [36] J. Zaanen, Planckian dissipation, minimal viscosity and the transport in cuprate strange metals, *SciPost Phys.* **6**, 061 (2019).
- [37] G. Baker, D. Valentinis, and A. P. Mackenzie, On non-local electrical transport in anisotropic metals, *Low Temp. Phys.* **49**, 1338 (2023).
- [38] G. Baker, T. W. Branch, J. S. Bobowski, J. Day, D. Valentinis, M. Oudah, P. McGuinness, S. Khim, P. Surówka, Y. Maeno, T. Scaffidi, R. Moessner, J. Schmalian, A. P. Mackenzie, and D. A. Bonn, Nonlocal electrodynamics in ultrapure PdCoO₂, *Phys. Rev. X* **14**, 011018 (2024).
- [39] C. Q. Cook and A. Lucas, Electron hydrodynamics with a polygonal Fermi surface, *Phys. Rev. B* **99**, 235148 (2019).
- [40] G. Varnavides, A. S. Jermyn, P. Anikeeva, C. Felser, and P. Narang, Electron hydrodynamics in anisotropic materials, *Nat. Commun.* **11**, 4710 (2020).
- [41] P. J. Ledwith, H. Guo, and L. Levitov, The hierarchy of excitation lifetimes in two-dimensional Fermi gases, *Ann. Phys.* **411**, 167913 (2019).
- [42] See Supplemental Material at URL-will-be-inserted-by-publisher.
- [43] H. Takatsu, J. J. Ishikawa, S. Yonezawa, H. Yoshino, T. Shishidou, T. Oguchi, K. Murata, and Y. Maeno, Extremely large magnetoresistance in the nonmagnetic metal PdCoO₂, *Phys. Rev. Lett.* **111**, 056601 (2013).
- [44] R. S. Markiewicz, S. Sahrakorpi, M. Lindroos, H. Lin, and A. Bansil, One-band tight-binding model parametrization of the high- T_c cuprates including the effect of k_z dispersion, *Phys. Rev. B* **72**, 054519 (2005).
- [45] J. Hofmann and U. Gran, Anomalously long lifetimes in two-dimensional fermi liquids, *Phys. Rev. B* **108**, L121401 (2023).
- [46] S. Kryhin and L. Levitov, Collinear scattering and long-lived excitations in two-dimensional electron fluids, *Phys. Rev. B* **107**, L201404 (2023).
- [47] Q. Hong, M. Davydova, P. J. Ledwith, and L. Levitov, Superscreening by a retroreflected hole backflow in tomographic electron fluids, *Phys. Rev. B* **109**, 085126 (2024).

Supplemental material to “Transverse voltage in anisotropic hydrodynamic conductors”

Kaize Wang,^{1,*} Chunyu Guo,¹ Philip J. W. Moll,^{1,†} and Tobias Holder^{2,‡}

¹*Max Planck Institute for the Structure and Dynamics of Matter, Hamburg 22761, Germany*

²*School of Physics and Astronomy, Tel Aviv University, Tel Aviv 69978, Israel*

In the supplemental material (SM), we provide comprehensive details on the derivation of the Boltzmann kinetic approach for anisotropic Fermi surfaces. We introduce the a suitable Dirac notation for the phase space variables an account of the numerical solver. Then we derive the transverse voltage decomposition, discuss the ballistic limit and finally document the various model systems which we were investigated in the main text.

CONTENTS

A. Dirac notation in phase space and collision operators	1
B. Boltzmann equation and numeical solution	4
C. Transverse voltage decomposition	5
D. Symmetric and anti-symmetric component of transverse voltage	7
E. Extreme ballistic limit	8
F. Channel current profile and longitudinal conductance for C_4 model	9
G. Continuous and tight-binding models for realistic systems	10
References	10

Appendix A: Dirac notation in phase space and collision operators

It is convenient to work with Dirac notations in Boltzmann transport equations to simplify things and avoid ambiguities [1, 2]. In the main text of the paper, we are considering two-dimensional Fermi liquids at zero temperature. Suppose the distribution function $f(\mathbf{r}, \mathbf{p}, t)$ is known. Then, for an arbitrary function $g(\mathbf{r}, \mathbf{p}, t)$ (here, g can denote for example velocity, energy, displacement,...), the expectation value of g is

$$\langle g \rangle = \int \frac{d\mathbf{r}d\mathbf{p}}{(2\pi\hbar)^2} g(\mathbf{r}, \mathbf{p}, t) f(\mathbf{r}, \mathbf{p}, t). \quad (\text{A1})$$

We can define the density of the above quantity by

$$\langle g(\mathbf{r}) \rangle = \int \frac{d\mathbf{p}}{(2\pi\hbar)^2} g(\mathbf{r}, \mathbf{p}, t) f(\mathbf{r}, \mathbf{p}, t). \quad (\text{A2})$$

Within a linearized ansatz for the Boltzmann equation, the distribution function is usually parametrized as

$$f(\mathbf{r}, \mathbf{p}, t) = f^0(\epsilon(\mathbf{p})) - E_F \partial_\epsilon f^0 h(\mathbf{r}, \mathbf{p}, t), \quad (\text{A3})$$

where $h(\mathbf{r}, \mathbf{p}, t)$ is a continuous and differentiable function. In a channel geometry, due to the translational invariance in the channel direction (direction x), the only remaining spatial variable is y . At zero temperaure, the Fermi function derivative is $\partial_\epsilon f^0 = -\delta(\epsilon_{\mathbf{p}} - E_F)$. Putting these simplifications together, the density becomes ($\hbar = 1$),

$$\begin{aligned} \langle g(y) \rangle &= \int \frac{dpd\theta}{4\pi^2} p f(y, \mathbf{p}) g(y, \mathbf{p}) = \int \frac{dpd\theta}{4\pi^2} p f^{(0)}(\mathbf{p}) g(y, \mathbf{p}) + E_F \int \frac{dpd\theta}{4\pi^2} p \delta(\epsilon_{\mathbf{p}} - \mu) h(y, \theta) g(y, \mathbf{p}) \\ &= E_F \int \frac{d\theta}{4\pi^2} \frac{p_F(\theta)}{|\partial_p \epsilon(\theta)|} h(y, \theta) g(y, \theta) \\ &= E_F \int \frac{d\theta}{4\pi^2} \frac{p_F^2(\theta)}{|\mathbf{v}_F(\theta) \cdot \mathbf{p}_F(\theta)|} h(y, \theta) g(y, \theta) \end{aligned} \quad (\text{A4})$$

where in the second line we assumed that g is a non-equilibrium quantity which vanishes at equilibrium, while in the third line we use the fact that

$$\partial_p \epsilon = \partial_{p_x} \epsilon \cdot \partial_{p_x} p_x + \partial_{p_y} \epsilon \cdot \partial_{p_y} p_y = \frac{v_x p_x + v_y p_y}{p}. \quad (\text{A5})$$

From Eq. (A4), we identify the measure in phase space as

$$A(\theta) = \frac{p_F^2 E_F}{4\pi^2 |\mathbf{v}_F(\theta) \cdot \mathbf{p}_F(\theta)|}. \quad (\text{A6})$$

In this way we can define bra-kets, thereby writing Eq. (A4) as an inner product. Namely, for any function $g(y, \theta)$, the corresponding ket and inner product are defined as

$$\begin{aligned} |g(y)\rangle &\equiv \int_0^{2\pi} d\theta \sqrt{A(\theta)} g(\theta, y) |\theta\rangle \\ \langle \theta' | \theta \rangle &= \delta(\theta - \theta'). \end{aligned} \quad (\text{A7})$$

which leads to the very compact form $\langle h|g\rangle$ for Eq. (A4). Likewise, for any linear operator \hat{Q} one can write

$$Q(y, y') = \int d\theta d\theta' \sqrt{A(\theta)} Q(y, y', \theta, \theta') \frac{1}{\sqrt{A(\theta')}} |\theta\rangle \langle \theta'| \quad (\text{A8})$$

Taking this convention, the distribution function and important modes like particle number c momentum p_i and velocity v_i are given by

$$|h(y)\rangle = \int dy d\theta \sqrt{A(\theta)} h(y, \theta) |\theta\rangle, \quad (\text{A9})$$

$$|c\rangle \equiv \frac{1}{\sqrt{N}} \int d\theta \sqrt{A(\theta)} |\theta\rangle, \quad (\text{A10})$$

$$|p_i\rangle \equiv \frac{1}{\sqrt{\langle p_i^2 \rangle}} \int d\theta \sqrt{A(\theta)} p_i(\theta) |\theta\rangle, \quad (\text{A11})$$

$$|v_i\rangle \equiv \int d\theta \sqrt{A(\theta)} v_i(\theta) |\theta\rangle. \quad (\text{A12})$$

where $i = 1, 2$ denotes x and y . Furthermore,

$$\begin{aligned} p_i(\theta) &= \mathbf{p}_F(\theta) \cdot \hat{x}_i, v_i(\theta) = \mathbf{v}_F(\theta) \cdot \hat{x}_i, \\ \langle p_i^2 \rangle &\equiv \int d\theta A(\theta) p_i^2(\theta), \\ N &\equiv \int d\theta A(\theta). \end{aligned} \quad (\text{A13})$$

The current therefore becomes

$$\langle J_i \rangle = \int dy \langle v_i \rangle(y) |y\rangle = \langle v_i | h \rangle. \quad (\text{A14})$$

In order to construct the collision operator, it is necessary to first prove the orthogonality of the modes Eq. (A11) and (A12) for a Fermi surface possessing $C_{n \geq 4}$ symmetry. To this end, we will use the fact that $\varepsilon_{\mathbf{k}} = \varepsilon_{-\mathbf{k}} \Rightarrow p_F(\theta) = p_F(\theta \pm \pi)$, $\mathbf{v}_F(\theta) = -\mathbf{v}_F(\theta \pm \pi)$, $A(\theta) = A(\theta \pm \pi)$.

$$\begin{aligned} \langle c|c\rangle &= \frac{1}{N} \int_0^{2\pi} A(\theta) d\theta = 1, \\ \langle c|p_i\rangle &\sim \int_0^{2\pi} d\theta A(\theta) p_\theta p_i(\theta) = \int_0^\pi d\theta A(\theta) p_\theta [p_i(\theta) + p_i(\theta - \pi)] = 0, \\ \langle p_i|p_i\rangle &= 1. \end{aligned} \quad (\text{A15})$$

These considerations would actually also apply for the less symmetric case C_2 rotational symmetry. However, in order to prove the relation $\langle p_i | p_j \rangle = \delta_{ij}$, we do need C_{2m} ($m \geq 2$) symmetry, which allows us to employ that

$$p_F(\theta) = p_F\left(\theta + \frac{\pi}{m}\right). \quad (\text{A16})$$

The C_{2m} symmetry for Fermi velocity therefore leads to

$$\begin{aligned} v_i(R\mathbf{k}) &= \frac{\epsilon(R\mathbf{k} + \delta k \hat{x}_i) - \epsilon(R\mathbf{k})}{\delta k}, \\ &= \frac{\epsilon(R(\mathbf{k} + \delta k R^{-1} \hat{x}_i)) - \epsilon(R\mathbf{k})}{\delta k}, \\ &= \frac{\epsilon(\mathbf{k} + [R^{-1} \hat{x}_i] \delta k) - \epsilon(\mathbf{k})}{\delta k} \\ &= \mathbf{v}(\mathbf{k}) \cdot [R^{-1} \hat{x}_i]. \end{aligned} \quad (\text{A17})$$

where R is an arbitrary two-dimension rotation matrix. Generally for any C_n ($n \geq 3$) symmetry,

$$\begin{aligned} v_x\left(\theta + \frac{2\pi}{n}j\right) &= \cos\left(\frac{2\pi}{n}j\right)v_x(\theta) - \sin\left(\frac{2\pi}{n}j\right)v_y(\theta), \\ v_y\left(\theta + \frac{2\pi}{n}j\right) &= \sin\left(\frac{2\pi}{n}j\right)v_x(\theta) + \cos\left(\frac{2\pi}{n}j\right)v_y(\theta), \\ p_x\left(\theta + \frac{2\pi}{n}j\right) &= p_x \cos\left(\frac{2\pi}{n}j\right) - p_y \sin\left(\frac{2\pi}{n}j\right), \\ p_y\left(\theta + \frac{2\pi}{n}j\right) &= p_y \cos\left(\frac{2\pi}{n}j\right) + p_x \sin\left(\frac{2\pi}{n}j\right) \end{aligned} \quad (\text{A18})$$

which means in particular that

$$A\left(\theta + \frac{2\pi}{n}j\right) = A(\theta). \quad (\text{A19})$$

We can insert this in the measure to obtain

$$\begin{aligned} \langle v_x | v_y \rangle &= \int_0^{2\pi} d\theta A(\theta; \mu) v_x(\theta) v_y(\theta), \\ &= \int_0^{\frac{2\pi}{n}} A(\theta; \mu) \sum_{j=0}^{n-1} \frac{v_x^2(\theta) - v_y^2(\theta)}{2} \sin\left(\frac{4\pi}{n}j\right) + v_x(\theta) v_y(\theta) \cos\left(\frac{4\pi}{n}j\right), \\ &= 0. \end{aligned} \quad (\text{A20})$$

In the final line, as explained we use

$$\sum_{j=0}^{n-1} \exp\left[i\frac{4\pi}{n}j\right] = 0 \quad (n \geq 3) \quad (\text{A21})$$

Similarly identity also holds for the orthogonality relation to particle density modes. In summary, for $C_{2m \geq 4}$ system, the orthogonal conditions are

$$\begin{aligned} \langle c | c \rangle &= \langle p_i | p_i \rangle = 1 \\ \langle c | p_i \rangle &= \langle c | v_i \rangle = 0 \\ \langle p_i | p_k \rangle &= \langle p_i | v_k \rangle = \langle v_i | p_k \rangle = \langle v_i | v_k \rangle = 0 \quad (j \neq k). \end{aligned} \quad (\text{A22})$$

The collision operators can therefore be constructed as

$$\begin{aligned} C_{\text{mc}} |h\rangle &= -\gamma_{\text{mc}} |h\rangle + \gamma_{\text{mc}} \langle c | h \rangle |c\rangle + \sum_i \gamma_{\text{mc}} \langle p_i | h \rangle |p_i\rangle, \\ C_{\text{mr}} |h\rangle &= -\gamma_{\text{mr}} |h\rangle + \gamma_{\text{mr}} \langle c | h \rangle |c\rangle, \end{aligned} \quad (\text{A23})$$

which obey

$$\begin{aligned}\langle c | C_{\text{full}} | h \rangle &= 0 \quad \text{Particle number conservation,} \\ \langle p_i | C_{\text{mc}} | h \rangle &= 0 \quad \text{Momentum conservation.}\end{aligned}\tag{A24}$$

This establishes an explicit construction of the collision terms in the Boltzmann equations which obeys the necessary conservation laws.

Appendix B: Boltzmann equation and numerical solution

The Boltzmann equation is

$$\left[\partial_t + \dot{\mathbf{p}} \cdot \nabla_{\mathbf{p}} + \dot{\mathbf{x}} \cdot \nabla_{\mathbf{r}} \right] f(\mathbf{x}, \mathbf{p}, t) = C[f].\tag{B1}$$

For a single band topologically trivial system, the stationary solution satisfies

$$\left[\mathbf{F} \cdot \nabla_{\mathbf{p}} + \mathbf{v}(\mathbf{p}) \cdot \nabla_{\mathbf{r}} \right] f(\mathbf{x}, \mathbf{p}) = C[f],\tag{B2}$$

where $\mathbf{v}(\mathbf{p}) = \partial_{\mathbf{p}} \epsilon(\mathbf{p})$ and in the presence of electric field, $\mathbf{F} = -e\mathbf{E}$. In our calculation, we fix the longitudinal electric field E_x and view $E_y(y)$ as a response to the input field E_x . Taking the linearized ansatz in Eq. (A3) and only considering linear response to the external field E_x , the Boltzmann equation for $h(y, \theta)$ reduces to the form mentioned in Eq. (3) in the main text,

$$\partial_y |v_y h\rangle - E_x |v_x\rangle - E_y(y) |v_y\rangle = C_{\text{full}} |h\rangle.\tag{B3}$$

In order to solve the above equation numerically, we write

$$\partial_y |v_\mu h\rangle + \gamma |h\rangle = \underbrace{E_x |v_x\rangle + E_y(y) |v_y\rangle + \gamma \langle c|h\rangle |c\rangle + \sum_{i=1,2} \gamma_{\text{mc}} \langle p_i|h\rangle |p_i\rangle}_{S[h]}\tag{B4}$$

In the absence of magnetic field, the BTE thus becomes

$$\left(v_y \partial_y + \gamma \right) h(y, \theta) = [E_x v_x(\theta) + E_y(y) v_y(\theta) + \gamma h_0(y) Y_0(\theta) + \gamma_{\text{mc}} \sum_{i=1}^2 h_i(y) Y_i(\theta)] \equiv S(y, \theta).\tag{B5}$$

Using a variable change to the characteristics,

$$\begin{aligned}\partial_s y &= v_y, & y(0) &= \text{sgn}(\mathbf{v}_\theta \cdot \hat{y}) \frac{w}{2} \\ \partial_s \theta &= 0, & \theta(0) &= \xi,\end{aligned}\tag{B6}$$

the BTE simplifies to

$$(\partial_s + \gamma) h(s, \xi) = S(s, \xi)\tag{B7}$$

By choosing a fully diffusive boundary condition,

$$h(0, \xi) = 0.\tag{B8}$$

the formal solution of the BTE reads

$$h(s, \xi) = \int_0^\infty ds' \Theta(s - s') e^{-\gamma(s-s')} S[h(s', \xi)].\tag{B9}$$

The solution Eq. (B9) can be expressed in the original variables $h(y, \theta)$ via the transformation

$$\begin{aligned}\xi &= \theta, \\ s &= \frac{y + \text{sgn}(\mathbf{v}_\theta \cdot \hat{y}) \frac{w}{2}}{\mathbf{v}_\theta \cdot \hat{y}}.\end{aligned}\tag{B10}$$

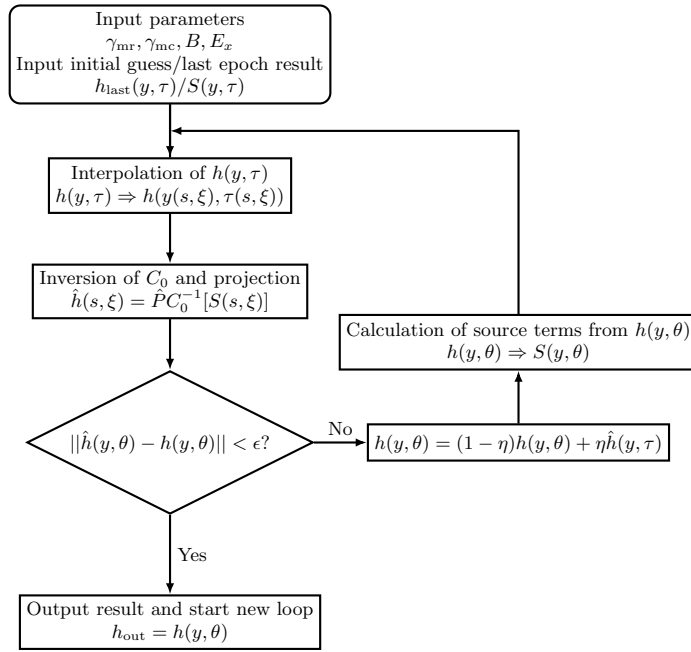


Figure 1. Flow chart of the numerical routine used to solve the BTE.

However, since the function S depends explicitly on h , additional constraints need to be fulfilled to select a physical solution. The most important constraint is of course charge conservation,

$$\partial_t \rho + \nabla \cdot \mathbf{J} = 0 \quad (\text{B11})$$

We furthermore enforce the constraint $J_y(\pm W/2) = 0$ to ensure that no current can leak outside of the channel. For stationary states and zero magnetic field, this combines with Eq.(B11) to give a vanishing J_y for all values of y .

Numerically, the solution to the BTE is constructed by iterating (B9) and imposing a projection of current J_y to eliminate the transverse current as follows,

$$|h^{\text{New}}\rangle = (\mathbb{1} - |v_y\rangle\langle v_y|) |h^{\text{Old}}\rangle. \quad (\text{B12})$$

A good starting point is to assume $S(y, \theta) = E_x v_x(\theta)$. Then

$$h^0(y, \theta) = \frac{E_x(\mathbf{v}_\theta \cdot \hat{x})}{\gamma} \left[1 - \exp\left(-\gamma \frac{2 \operatorname{sgn}(\mathbf{v}_\theta \cdot \hat{y}) y + w}{2|\mathbf{v}_\theta \cdot \hat{y}|}\right) \right]. \quad (\text{B13})$$

The numerical flow chart is summarized in Fig. 1. As a benchmark, we compare our calculation result to Ref. [3] in Fig. 2. The agreement is excellent in the Gurzhi region, but we note that the solver was not optimized for the deep hydrodynamic limit, where it converges very slowly.

Appendix C: Transverse voltage decomposition

In order to obtain transverse voltage, we can either act with the bra $\langle v_y|$ or alternatively with $\langle p_y|$ from the left in Eq. (B4). Utilizing Eq. (A22) one can then immediately solve for E_y .

By contracting with $\langle p_y|$, we obtain

$$E_y = \frac{\partial_y \langle p_y v_y \rangle + \gamma_{\text{mr}} \langle p_y \rangle}{\langle p_y | v_y \rangle} \quad (\text{C1})$$

$$\equiv \frac{\partial_y \Pi_{yy} + \gamma_{\text{mr}} p_y(y)}{\langle p_y | v_y \rangle}, \quad (\text{C2})$$

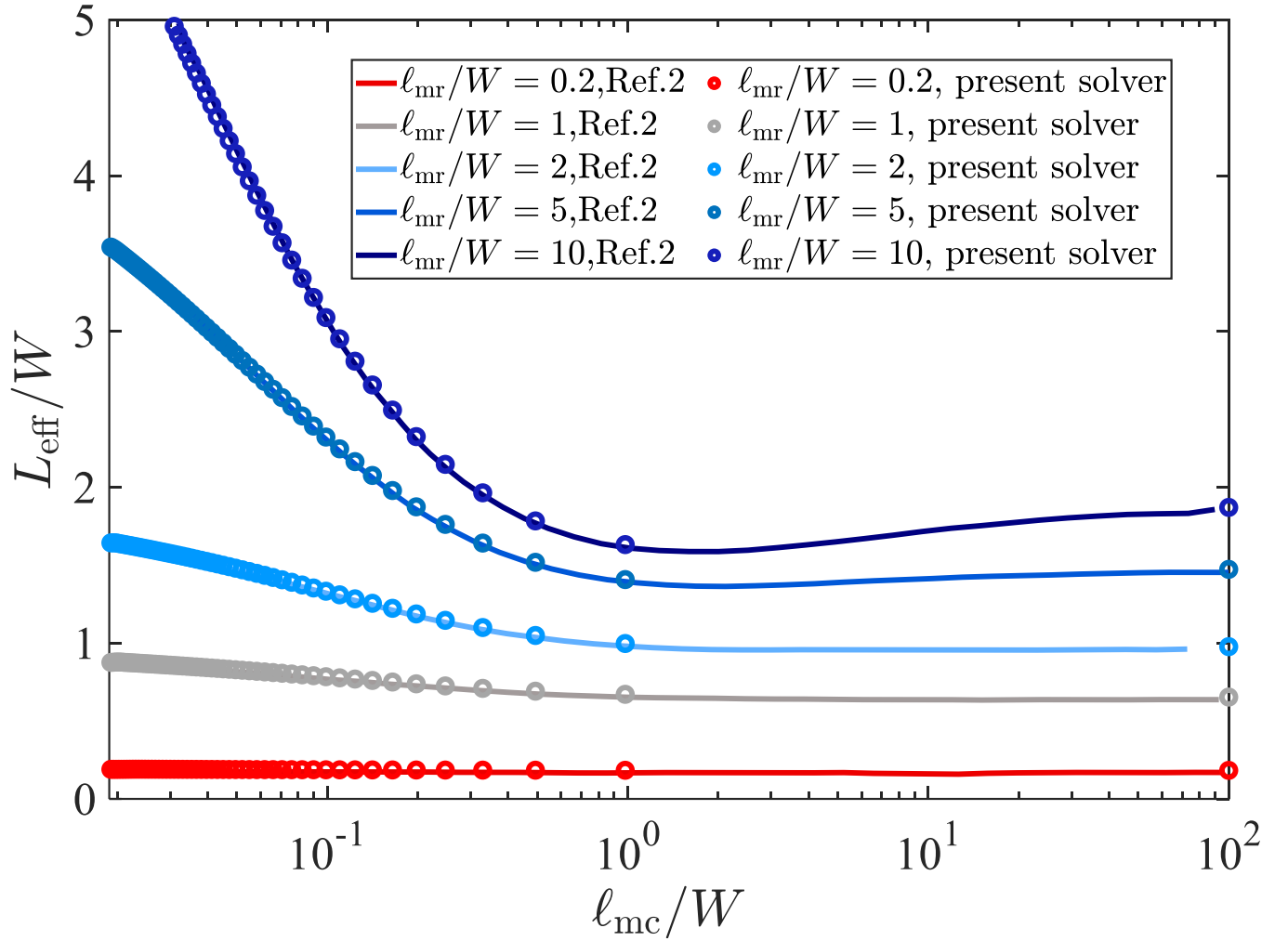


Figure 2. Comparison between our BTE solver to the previous results in Ref. [3].

where Π is the stress tensor of a quantum fluid [4, 5] and $p_y(y)$ is the momentum density. Integrating over y , we yield the transverse voltage

$$\Phi_y = \frac{1}{\langle p_y | v_y \rangle} \left(\Pi_{yy} \Big|_{-W/2}^{W/2} + \gamma_{mr} P_y \right). \quad (\text{C3})$$

This result clearly shows that in the hydrodynamic limit only the internal stress contributes to the transverse voltage, i. e. ($\gamma_{mr}/\gamma_{mc} \rightarrow 0$),

$$\Phi_y^{\text{hydro}} = \frac{1}{\langle p_y | v_y \rangle} \Pi_{yy} \Big|_{-W/2}^{W/2}. \quad (\text{C4})$$

Interestingly, the alternative way of decomposing Φ_y gives rise to the ballistic limit: By contracting with $\langle v_y |$, one obtains

$$E_y = \frac{\partial_y \langle v_y v_y \rangle - \gamma_{mc} \langle p_y \rangle}{\langle v_y | v_y \rangle} \quad (\text{C5})$$

$$\equiv \frac{\partial_y \Sigma_{yy} - \gamma_{mc} p_y(y)}{\langle v_y | v_y \rangle}, \quad (\text{C6})$$

where $\Sigma_y y = \langle v_y v_y \rangle$ is the velocity-velocity correlator. Integrating over y , this becomes

$$\Phi_y = \frac{1}{\langle v_y | v_y \rangle} \left(\Sigma_{yy} \Big|_{-W/2}^{W/2} - \gamma_{mc} P_y \right) \quad (\text{C7})$$

As promised, in the ballistic limit ($\gamma_{mc} = 0$), the transverse voltage is given by

$$\Phi_y^{\text{ball}} = \frac{1}{\langle v_y | v_y \rangle} \Sigma_{yy} \Big|_{-W/2}^{W/2}. \quad (\text{C8})$$

In the main text, we opted for the decomposition according to Eq. (C3) rather than Eq. (C7). The reason is straightforward, compared to the correlator Σ , whose properties are not well documented, the stress tensor Π has a clear physical interpretation. In particular, Π allows us to formulate a continuity equation for momentum $p_y(y)$, which reads

$$\frac{\partial p_y}{\partial t} = -\frac{\partial \Pi_{ij}}{\partial x_j} - \gamma_{mr} p_y + e E_y \quad (\text{C9})$$

In the steady state, the temporal derivative in (C9) vanishes, so that

$$e E_y = \gamma_{mr} p_y(y) + \partial_y \Pi_{yy}(y) \quad (\text{C10})$$

which leads us immediately to (C2) once the proper normalization is imposed.

Appendix D: Symmetric and anti-symmetric component of transverse voltage

For Fermi surface with C_{2m} symmetry, the irreducible misalignment angle domain is $\varphi \in [0, \pi/2m]$ since $\Phi_y(\varphi + \pi/2m) = -\Phi_y(\varphi - \pi/2m)$. The anisotropic nature of Fermi surface results in the Φ_y v.s. φ profile asymmetric, i.e. the maximum value of Φ_y does not coincide with $\varphi = \pi/4m$ (cf. main text Fig.2(c)). We then further look into the symmetric and anti-symmetric component of Φ_y w.r.t. φ in $[0, \pi/2m]$. They are defined as follows:

$$\begin{aligned} \Phi_y^a(\varphi) &= \frac{1}{2} [\Phi_y(\varphi) - \Phi_y(\pi/2m - \varphi)] \\ \Phi_y^s(\varphi) &= \frac{1}{2} [\Phi_y(\varphi) + \Phi_y(\pi/2m - \varphi)] \end{aligned} \quad (\text{D1})$$

In Fig. 3(a), we showed that for PdCoO₂, the anti-symmetric component is more susceptible to MC scattering and changes sign with smaller $\gamma_{mc} v_F / W \approx 0.2$. In Fig. 3(b) and (c), we clearly see that for $\gamma_{mc} v_F / W < 0.2$, the symmetric part is dominant and the whole transverse voltage does not change sign.

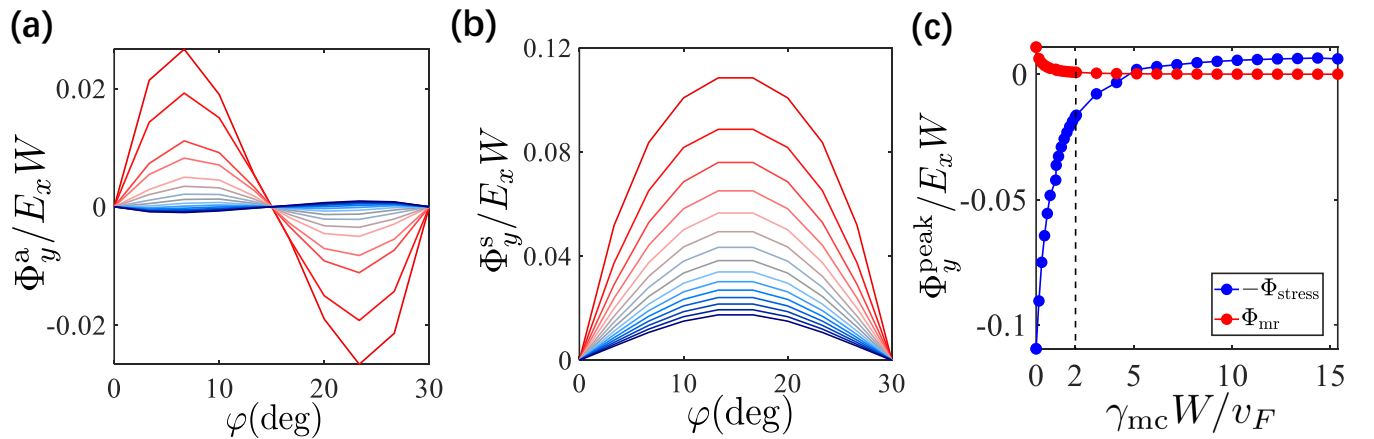


Figure 3. Transverse voltage plots for PdCoO₂ with same parameters as in Fig.4(b) in main text. (a)Anti-symmetric component of transverse voltage. (b)Symmetric component of transverse voltage. (c)Full transverse voltage decomposition. Black dash line is an eye guide to $\gamma_{mc} v_F / W = 0.2$.

This observation helps to identify a weaker hydrodynamic signature in real materials. The sign change of the anti-symmetric component of the transverse voltage could serve as an effective detector for broader experimental materials due to its earlier onset with the MC scattering rate.

Appendix E: Extreme ballistic limit

Here we show the results of a pure ballistic case and further explain Fig.2(b) in the main text. For ballistic case, $\gamma = \gamma_{\text{mr}}$, and the source term S is constituted only from electric field and particle number modes. As it turns out, we find that already for not too small γ_{mr} , solution (B13) is a good approximation to the full solution of distribution function. According to Eq. (C8), the transverse voltage can be written explicitly as

$$\Phi_y^{(0)} = \frac{2E_x}{\gamma} \frac{\int d\theta A(\theta) v_y^2(\theta) v_x(\theta) e^{-\gamma w/2|v_y|} \sinh\left(\frac{\gamma W}{2v_y}\right)}{\int d\theta A(\theta) v_y^2(\theta)}. \quad (\text{E1})$$

As shown in Fig. 4, this approximation and the numerical solution show the same qualitative behavior, meaning that Eq. (E1) can successfully capture **the sign** of the voltage.

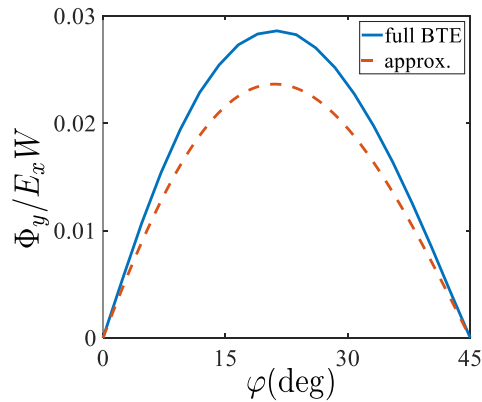


Figure 4. Comparison between a full solution and approximated analytic result, $\alpha = 0.4$.

For very small γ , Eq. (E1) reduces to

$$\Phi_y^{(0)} = -\frac{\gamma}{2} E_x W^2 \frac{\int d\theta A(\theta) v_x \text{sign}(v_y)}{\int d\theta A(\theta) v_y^2(\theta)}, \quad (\text{E2})$$

which allows us to read off what decides the sign of transverse voltage in the extreme ballistic limit, which is the average $\langle \text{sign}(v_y) v_x \rangle$. The physical content in this average is as follows: For a given electric field E_x , the response to it is trivially proportional to v_x , while $\text{sign}(v_y)$ counts whether the electrons move to the top/bottom in the transverse direction of the channel. The resulting voltage plot as a function of α is shown in Fig. 5, where the sign change is at $\alpha_c \approx 0.3$, very similar to the sign change shown in Fig.2(b) of the main text, which was obtained from the full calculation.

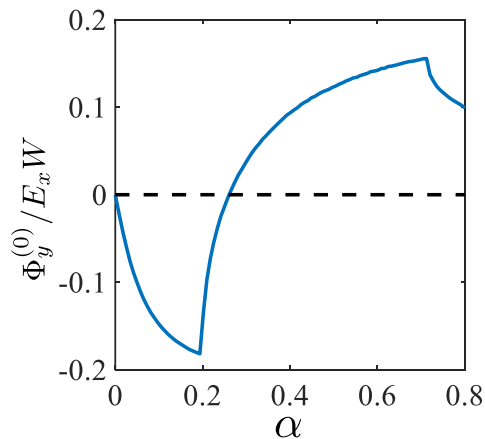


Figure 5. Transverse voltage according to Eq. (E2) based on the quantity $\text{sign}(v_y)v_x$. Parameters are the same as in main text Fig. 2(b).

Appendix F: Channel current profile and longitudinal conductance for C_4 model

Here we show the longitudinal conductance G for our C_4 model with different Fermi surface anisotropy α in Fig. 6. The conductance G is defined as

$$G = \int dy J_x(y)/E_x. \quad (\text{F1})$$

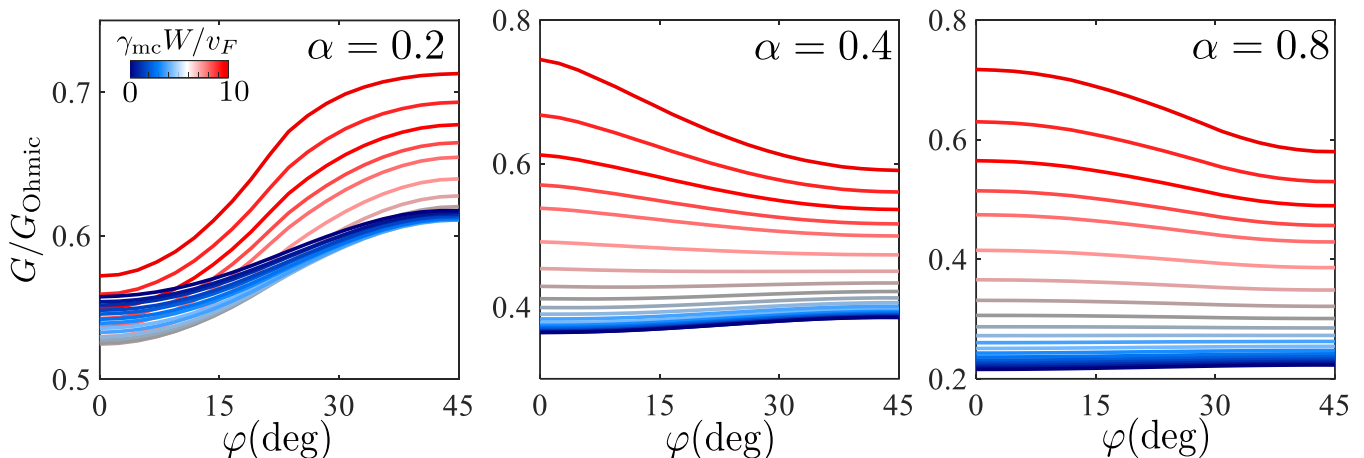


Figure 6. Conductance G as a function of different misalignment angles φ and MC scattering rate γ_{mc} for different α . Here, all $\gamma_{\text{mr}}W/v_F = 1$.

Firstly, the conductance is varied with changing misalignment angles, showing its extreme values at high symmetry positions ($\varphi = 0^\circ, 45^\circ$). We observed quite different behavior of the conductance with varying Fermi surface anisotropy. Looking at $\alpha = 0.4, 0.8$, from the ballistic to the hydrodynamic limit, the conductance at a fixed misalignment angle decreases consistently. On the other hand, $\alpha = 0.2$ leads to crossings between different lines, meaning different misaligned configuration lead to different relationships with respect to γ_{mc} . It is evident that the anisotropy of the Fermi surface leads to different scaling behaviors (at least scaling with ℓ_{mc}) for different Fermi surfaces. This finding further supports the conclusions drawn in the main text that anisotropic Fermi surfaces can lead to qualitatively different flow behavior, and it calls into question how generally applicable some of the results for an isotropic model are when compared to real materials.

Appendix G: Continuous and tight-binding models for realistic systems

The models used in main text Fig.4 of realistic systems are presented here.

a. The continuous C_4 model is a real band dispersion for the geometrical C_4 model discussed in Fig.(2) of main text. The energy dispersion is $\epsilon(\mathbf{k}) = k^2/2m - 2t(k_x^4 + k_y^4 - 6k_x^2k_y^2)/k^4 - \mu$ with parameters $m = 0.5, t = 1, \mu = 1$.

b. The Square model is a simple tight-binding model at nearly half-filled. The energy dispersion is $\epsilon(\mathbf{k}) = -2t(\cos k_x + \cos k_y) - \mu$ with parameters $t = 1, \mu = -0.1$.

c. The PdCoO₂ model describes the in-plane dispersion of PdCoO₂, ignoring the small corrugation along k_z direction [6]. The energy dispersion is

$$\epsilon(\mathbf{k}) = -2t_1\{\cos(\mathbf{k} \cdot \mathbf{a}) + \cos(\mathbf{k} \cdot \mathbf{b}) + \cos[\mathbf{k} \cdot (\mathbf{a} + \mathbf{b})]\} - 2t_2\{\cos^2(\mathbf{k} \cdot \mathbf{a}) + \cos^2(\mathbf{k} \cdot \mathbf{b}) + \cos^2[\mathbf{k} \cdot (\mathbf{a} + \mathbf{b})]\}, \quad (\text{G1})$$

with parameters $\mathbf{a} = \hat{x}, \mathbf{b} = \frac{1}{2}(\hat{x} + \sqrt{3}\hat{y}), t_1 = 1, t_2 = 0.14$.

d. The Bi2212 model describes the in-plane dispersion of overdoped cuprate Bi₂Sr₂CaCu₂O₈, ignoring the small corrugation along k_z direction [7]. For convenience, define $c_i(\alpha a) = \cos(\alpha k_i a)$. The energy dispersion is $\epsilon(\mathbf{k}) = -2t_1[c_x(a) + c_y(a)] - 4t_2c_x(a)c_y(a) - 2t_3[c_x(2a) + c_y(2a)] - 2t_4[c_x(2a)c_y(a) + c_y(2a)c_x(a)]$ with parameters $a = 1, t_1 = 1, t_2 = -0.135, t_3 = 0.061, t_4 = -0.017$.

* kaize.wang@mpsd.mpg.de

† philip.moll@mpsd.mpg.de

‡ tobiasholder@tauex.tau.ac.il

- [1] C. Q. Cook and A. Lucas, Electron hydrodynamics with a polygonal Fermi surface, *Phys. Rev. B* **99**, 235148 (2019).
- [2] P. J. Ledwith, H. Guo, and L. Levitov, The hierarchy of excitation lifetimes in two-dimensional Fermi gases, *Ann. Phys.* **411**, 167913 (2019).
- [3] M. J. M. de Jong and L. W. Molenkamp, Hydrodynamic electron flow in high-mobility wires, *Phys. Rev. B* **51**, 13389 (1995).
- [4] B. Bradlyn, M. Goldstein, and N. Read, Kubo formulas for viscosity: Hall viscosity, Ward identities, and the relation with conductivity, *Phys. Rev. B* **86**, 245309 (2012).
- [5] P. Massignan, G. M. Bruun, and H. Smith, Viscous relaxation and collective oscillations in a trapped fermi gas near the unitarity limit, *Physical Review A* **71**, 033607 (2005).
- [6] H. Takatsu, J. J. Ishikawa, S. Yonezawa, H. Yoshino, T. Shishidou, T. Oguchi, K. Murata, and Y. Maeno, Extremely large magnetoresistance in the nonmagnetic metal PdCoO₂, *Phys. Rev. Lett.* **111**, 056601 (2013).
- [7] R. S. Markiewicz, S. Sahrakorpi, M. Lindroos, H. Lin, and A. Bansil, One-band tight-binding model parametrization of the high- T_c cuprates including the effect of k_z dispersion, *Phys. Rev. B* **72**, 054519 (2005).